JOM, Vol. 66, No. 7, 2014
DOI: 10.1007/s11837-014-1011-2


# Integrated Computational Materials Engineering (ICME) Approach to Design of Novel Microstructures for Ti-Alloys

DONG WANG,[1,2] RONGPEI SHI,[1] YUFENG ZHENG,[1]
RAJARSHI BANERJEE,[2] HAMISH L. FRASER,[1] and YUNZHI WANG[1,3]

1.—Department of Materials Science and Engineering, The Ohio State University, 2041 N. College Rd., Columbus, OH, USA. 2.—Department of Materials Science and Engineering, University of North Texas, Denton, TX, USA. 3.—e-mail: wang.363@osu.edu

In this overview, we present integrated CAPHAD and phase-field modeling with critical experiments to explore a newly discovered, nonconventional, solid–solid phase transformation pathway based on the so-called pseudo-spinodal mechanism. We show that this new transformation pathway offers a new design strategy for Ti alloys with extremely fine and uniform $\alpha + \beta$ microstructures that could potentially have highly attractive balances of mechanical properties. To broaden the processing window for such a mechanism to operate, we also explore a different nonconventional transformation pathway that involves precursory phase separation. In addition, the variant selection process during the $\beta \rightarrow \alpha$ transformation leading to macrozones is investigated and the results could shed light on how to control processing conditions to avoid or reduce microtexture at both the individual $\beta$ grain level and the overall polycrystalline sample level.

## INTRODUCTION

Most engineering alloys for structural applications are strengthened by second-phase particles. Features such as the volume fraction, size, shape, orientation, coherency state, and spatial distribution of these particles characterize the microstructures of such alloys, and they profoundly influence the deformation mechanisms and mechanical behavior. Among these microstructural features, the density and nature of heterophase interfaces and their spatial uniformity are extremely important. Familiar examples include very high-strength structural Al alloys involving formation of Guinier–Preston–Bagaryatsky (GPB) zones at an extremely fine (atomic) scale,[1–3] high-strength and high-ductility steels with ultrafine (nanometer scale) lamellar structures consisting of either ferrite + cementite[4,5] or ferrite + austenite,[6] and Ni-base superalloys with refined (nanometer-scale) precipitates of the $L1_2$ $\gamma'$ phase (based on $Ni_3Al$).[7,8] In the case of Ti alloys, in the $\beta$-heat-treated condition, for example, the $\alpha$-phase usually forms both as an allotriomorph along prior $\beta$-grain boundaries and as Widmanstätten plates nucleating at the grain boundary $\alpha$-phase[9,10] or from an existing Widmanstätten plate,[10–12] leading to relatively coarse lamellar structures (e.g., Fig. 1a) with strong transformation texture (i.e., appearance of large regions of $\alpha$ plates consisting of the same crystallographic orientation variant or different variants but with a common crystallographic feature such as a common basal $(0001)_\alpha$ pole; these regions within individual $\beta$ grains or across grain boundaries are often referred to as "macrozones" or microtextured regions). These microstructural characteristics usually result in a significant reduction in the fatigue life of Ti alloy components.[13,14]

Generally in Ti alloys, it has not been possible to produce very refined microstructures with either no or limited microtexture, and balances of properties have been realized by either $\beta$-processing producing distributions of allotriomorphic $\alpha$-plates in either the colony (slow cooling) or basketweave (fast cooling) morphologies, or by $\alpha/\beta$ processing to distribute equiaxed $\alpha$-particles with so-called transformed $\beta$ regions. However, exciting recent theoretical[15,16] and experimental[17] developments provided opportunities to design ultrafine and ultrauniform $\alpha + \beta$ microstructure (Fig. 1c) via a new and nonconventional intragranular transformation pathway. This new transformation pathway is based on the

(Published online May 28, 2014)

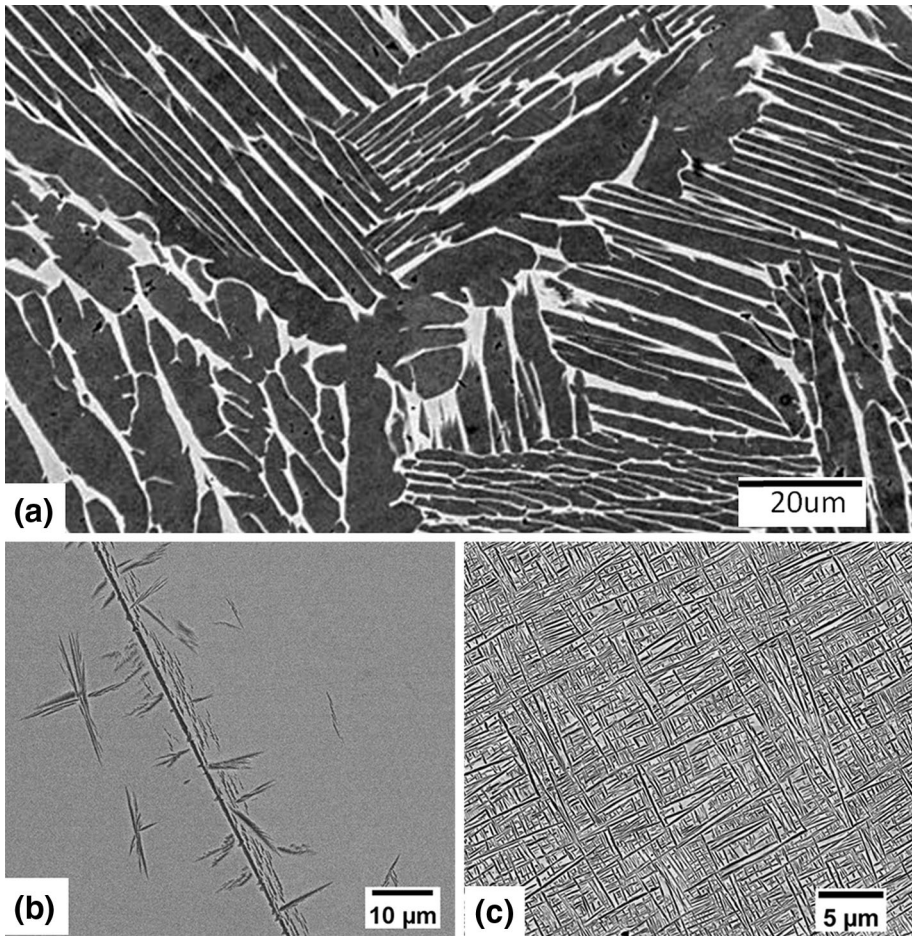


Fig. 1. (a) SEM micrograph of a typical $\alpha + \beta$ microstructure in Ti-6Al-4V (wt.%), being $\beta$-solutionized at 1020°C and then slowly cooled to room temperature at the rate of 1°C/min *white color* describe the Beta phase, and *black color* describe the alpha phase. (b and c) SEM backscattered images of Ti-5Al-5V-5Mo-3Cr-0.5Fe (wt. %) samples that were $\beta$-solutionized (1000°C/30 min), step quenched, and isothermally aged for 30 min at 700°C and isothermally aged for 30 min at 600°C, respectively *grey color* describe the Beta phase, and *black color* describe the alpha phase.

so-called pseudo-spinodal mechanism first proposed by Ni and Khachaturyan[15] to account for "tweed" microstructures. Furthermore, if we develop a better understanding of the variant selection process during the $\beta \rightarrow \alpha$ transformation that leads to the macrozones, we would be able to control the processing conditions to avoid or reduce microtexture at both the individual $\beta$ grain level and the overall polycrystalline sample level. There is, therefore, much anticipation regarding the development of attractive balances of properties in Ti alloys with ultrafine and ultrauniform precipitate microstructures free of transformation texture through transformation pathway engineering.

In this article, we present an Integrated Computational Materials Engineering (ICME) approach that could be used to accelerate the realization of the new transformation pathway and alloy design concept, and the optimization of processing conditions for close control of transformation texture in the development of the next generation of Ti alloys. These alloys will have extremely fine and uniform microstructures with little or no microtexture; therefore, substantially improved properties (e.g., an excellent combination of strength and ductility as well as high-temperature microstructural stability) are expected. In this approach, alloy development will be led by computational modeling to permit the rapid discovery of new types of alloys that may have been missed by the traditional trial-and-error method. In particular, we predict composition and temperature windows for the pseudo-spinodal intragranular transformation mechanism to operate by using a model alloy system. We also predict coupled microstructure and texture evolution due to variant selection under the influence of different processing variables during the $\beta \rightarrow \alpha$ transformation, including effects of dislocations, prestraining, type of boundary constraint, and starting texture of the $\beta$ samples. Our findings may shed light on the design of the next generation of Ti alloys (alloy chemistry and processing conditions) with ultrafine and uniform precipitate microstructures and hence potentially much improved balances of properties that may be exploited for application in components.

## METHOD

The nonconventional pseudo-spinodal transformation pathway mentioned above involves two phases having different compositions as well as different crystal structures. If the parent phase has a composition close to the intersection point of the free energy-composition curves of the parent and product phases (referred to as the $c_0(T)$ point for that particular temperature), then small concentration fluctuations will drive the composition of certain regions of the parent phase to the opposite side of the $c_0(T)$ point. The system can reduce its free energy by transforming these regions congruently to the product phase. Subsequently, long-range diffusional partitioning between the parent and product phases during isothermal annealing drives their compositions toward equilibrium. The operation of such a nonconventional transformation pathway is determined by the interplay between two competing structural and compositional instabilities within the $\beta$ matrix.[18] It is therefore necessary to tailor the relative strengths of these two instabilities by adjusting the alloy composition and heat-treatment schedule to promote or suppress a given pathway, which is rather difficult to do through trial-and-error experimentation because the mechanism may operate only in a narrow processing window.[16] For variant selection during $\beta \rightarrow \alpha$ transformation, which $\alpha$ variants have the smallest activation energy for nucleation and which ones have the fastest grow rate at a given moment in time is determined by the structural and chemical nonuniformities in the $\beta$ phase matrix and the stress state associated with these nonuniformities, as well as residual stress from prior thermomechanical processing (TMP) history. Then, the nucleation and growth of $\alpha$ precipitates taking place at the given moment will alter the existing microstructural and stress states and thus will change the variant selection process for the next increment in time. Thus, it is also extremely difficult to develop a fundamental understanding of such an intimately coupled process by trial-and-error experimentation alone.

From the computational materials engineering point of view, to describe microstructure evolution following the nonconventional intragranular transformation pathway and variant selection during precipitation, computational models must be able to treat homogeneous/continuous (such as congruent ordering, spinodal ordering, and decomposition)[18] and heterogeneous (conventional nucleation and growth) transformation mechanisms simultaneously. Models also should consider the effects of preexisting arbitrary structural and chemical nonuniformities (such as dislocations and grain boundaries, preexisting precipitates, and the presence of precursory phase separation, etc.) on nucleation. Based on gradient thermodynamics[19–21] and microelasticity theory,[22–26] the phase-field approach[27–33] (also called the diffuse-interface approach) offers an ideal framework to deal rigorously and realistically with these difficult challenges. In this approach, the total free energy (including the chemical, elastic, and interfacial energies) of an arbitrary heterogeneous system is formulated as a function of both the local chemical and structural states and their spatial variations (gradients). The minimum energy path (MEP) on the free-energy hypersurface then defines the transformation path(s) and microstructural states, regardless of whether spinodal decomposition or phase separation by nucleation and growth[34] is involved.

As has been demonstrated in a recent phase-field simulation study of the $\beta \rightarrow \alpha$ transformation in Ti-6Al-4V (in wt.%),[35,36] the formulation of the total free energy functional, which consists of the bulk chemical free energy, elastic strain energy, and interfacial energy, has accounted for the following: (I) reliable thermodynamic data for the bulk chemical free energy;[36,37] (II) crystallography of the $\beta \rightarrow \alpha$ crystal lattice rearrangement, including orientation relationship (OR) and lattice correspondence (LC) as functions of the lattice parameters of the precipitate and parent phases (i.e., the effect of alloy chemistry) note that LC also referred to as atomic site correspondence in diffusional transformation; (III) accommodation of the transformation strain; (IV) development of defect structures (misfit dislocations and structural ledges) at $\alpha/\beta$ interfaces as precipitates grow in size; and (V) elastic interaction of nucleating particles with existing chemical and structural nonuniformities and other stress-carrying defects such as dislocations.[38] In this article, we show that the nonconventional intragranular transformation pathway can be predicted by the phase-field method through coupling with CALPHAD (calculation of phase diagram) thermodynamic and mobility databases. Such a quantitative phase-field model can also be applied to study variant selection during the $\beta \rightarrow \alpha$ transformation. In combination with orientation distribution function (ODF) modeling[39,40] of the simulated $\alpha/\beta$ microstructures, the phase-field model allows for a treatment of both microtexture and macrotexture evolution accompanying $\alpha/\beta$ microstructure evolution during different thermomechanical treatments.

## DESIGN OF NOVEL *A*/*B* MICROSTRUCTURE THROUGH NONCONVENTIONAL TRANSFORMATION PATHWAYS

To investigate whether the pseudo-spinodal mechanism operates in Ti alloys and, if it does, to identify the processing window size (i.e., temperature range for a given alloy composition or alloy composition range at a given temperature) for designing ultrafine and ultrauniform $\alpha + \beta$ microstructures by using this mechanism, we start with a simple binary alloy system, Ti-Mo, for which a critically assessed thermodynamic database is available. Although this is a much simpler system compared with the commercial Ti alloys such as

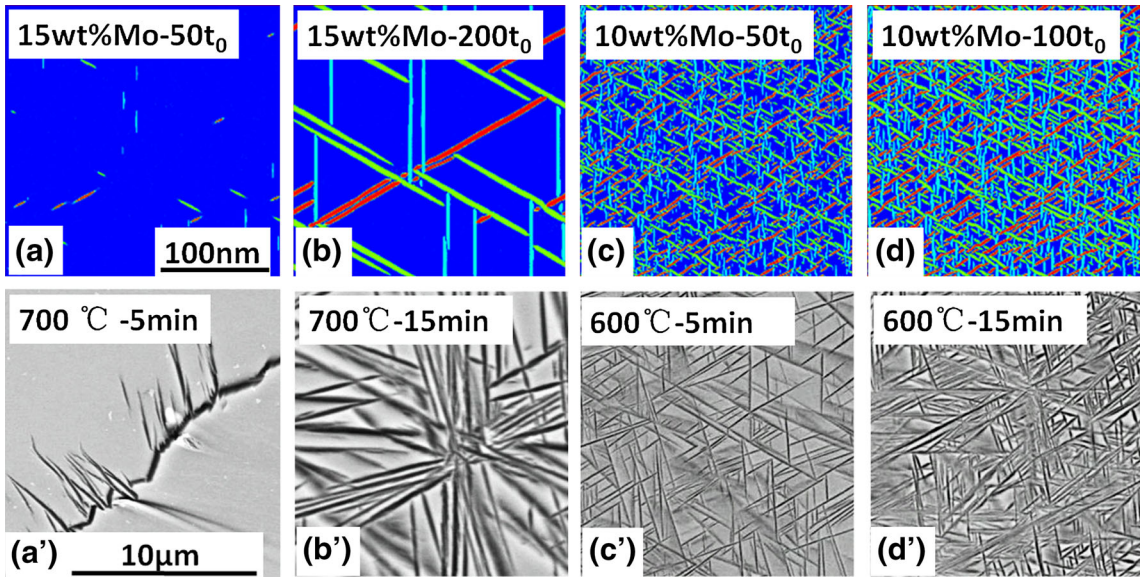


Fig. 2. Top row: Phase-field simulation prediction obtained using CALPHAD free energy models in PANDAT database, mobility database, and an interfacial energy of 100 mJ/m$^2$, isothermal aging at 600°C with two different Mo concentrations. Different colors represent different $\alpha$ variants. $t_0$ is the reduced time unit related to Mo diffusivity. Bottom row: backscatter SEM images from Ti-10Mo (in wt.%) after step quenching and isothermal holding at 700°C for 5 min and 15 min, and 600°C for 5 min and 15 min.

Ti-5553 (Ti-5Al-5V-5Mo-3Cr-0.5Fe) and $\beta$-21s (Ti-15Mo-3Al-2.7Nb-0.3Si) (composition in wt.%), the critical fundamental knowledge generated from this model alloy, such as the criteria that control the pseudo-spinodal mechanism, e.g., (I) how sensitive $c_0(T)$ is to alloy chemistry and (II) how close an alloy composition or an aging temperature has to be to $c_0(T)$ to involve the pseudo-spinodal mechanism rather than the conventional nucleation and growth, can guide the design of commercially important Ti alloys.

Using the free energy model in Thermo-Calc (Thermo-Calc Software Inc., McMurray, PA) and Pandat (CompuTherm LLC, Madison, WI)[41,42] for Ti-Mo alloys, the calculation of the $c_0(T)$ values is rather straightforward. They are 5.8 wt.% and 9.0 wt.% Mo respectively, at 700°C and 600°C.[17] Based on these values, we predict that an alloy of composition Ti-10 wt.% Mo is likely to follow the conventional nucleation and growth transformation pathway if quenched from above the $\beta$ transus and isothermally held at 700°C. However, if the same alloy is quenched and then isothermally held at 600°C, where the alloy composition will be quite close to $c_0(T)$, the transformation pathway may follow the pseudo-spinodal mechanism, leading to much finer scale intragranular distribution of $\alpha$ precipitates within the $\beta$ grains. The top row of Fig. 2 shows our preliminary phase-field simulation results in two dimensions (512 × 512 mesh points) for two alloys of different Mo concentrations, one close to $c_0(T = 600°C)$ and one far away from it, isothermally aged at $T = 600°C$ for different amounts of reduced time. The nucleation process is simulated by introducing thermal fluctuations in both concentration and structural order parameters using the Langevin random force approach.[43] The atomic mobilities or interdiffusion coefficient in Ti-Mo system at 600°C, e.g., $D = 10^{-18}$ m$^2$/s, can also be obtained from the CALPHAD approach.[44] For the phase-field mobility (i.e., the kinetic coefficient in the time-dependent Ginsburg-Landau equation), it has been chosen (i.e., $M = 6.0 \times 10^{-8}$ J/m$^3$/s) so as to guarantee a diffusion-controlled precipitation process, as detailed in Ref. [37]. In phase-field simulations, the length scale of the computational supercell is determined by the interfacial energy. In this study, we have assumed that the interfacial energy between the $\alpha$ and $\beta$ phases at the aging temperature is 100 mJ/m$^2$, which yields a submicron length scale.

We also prepared a Ti-10Mo alloy, homogenized and solution treated at 900°C (above the $\beta$ transus) and then directly step quenched to two different isothermal holding temperatures of 700°C and 600°C, respectively. The results are shown in the bottom row of Fig. 2. Both the simulation and experimental results reveal a substantially higher number density of $\alpha$ precipitates and hence much finer microstructures when the alloy composition is close to $c_0(T)$ compared with those obtained when the alloy composition is far from $c_0(T)$. These results indicate that there is a substantial difference between the mechanisms of $\alpha$ precipitation in the two cases, possibly being pseudo-spinodal decomposition in the former (see Fig. 3 for details) and conventional nucleation and growth in the latter. Similar behavior has also been observed in Ti-5553 as shown in Fig. 1b and c and $\beta$-21s.[16,17]

The quantitative characterization of the simulated microstructures[16] shows that the nucleation rate associated with the pseudo-spinodal mechanism

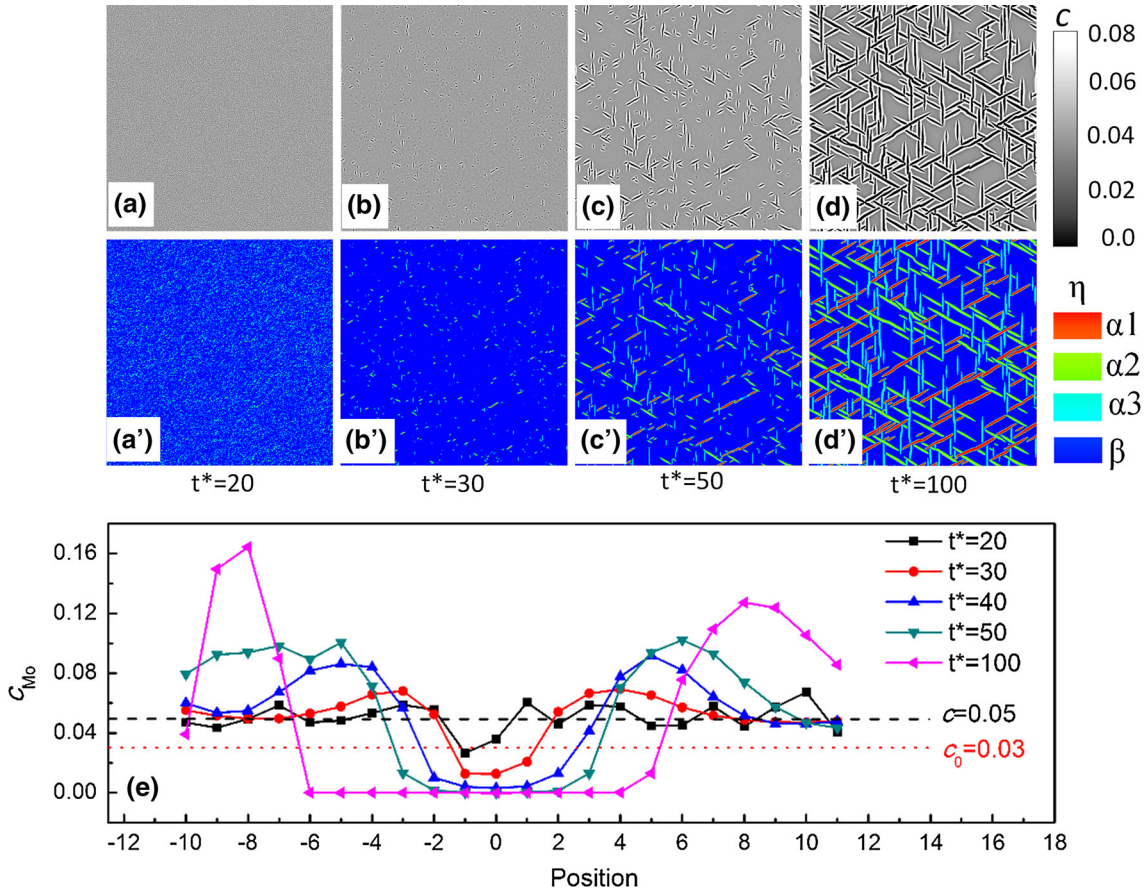


Fig. 3. Phase-field simulations (in two dimensions) of microstructural evolution during $\alpha$ precipitation via the pseudo-spinodal mechanism in Ti-5Mo (in wt.%) at 700°C. (a–d) show the concentration field in grayscale with dark shade representing low Mo concentration. (a′–d′) show the structural order parameter fields, with red, green, and light blue representing the three variants of $\alpha$ precipitates and blue representing the $\beta$ phase. The Langevin noise terms simulating thermal fluctuations were turned off after $t^* = 20$. (e) Typical concentration profile change across an $\alpha$ precipitate during its growth at different moments of time $t^*$, where $t^*$ is a dimensionless time unit reduced by Mo mobility.

is ~100 times that expected from the conventional nucleation and growth mechanism estimated using the classic nucleation theory.[16,45] When the alloy composition is far from $c_0(T)$, the nucleation rate obtained from the phase-field simulations is more or less in line with that predicted by classic nucleation theory. It is found for Ti-Mo that the alloy composition has to be within about 2 wt.% of $c_0(T)$ (either by adjusting alloy composition or by adjusting aging temperature) to involve the pseudo-spinodal mechanism effectively.

These simulation predictions demonstrate clearly that the pseudo-spinodal mechanism does offer a new way to produce extremely refined and uniform $\alpha + \beta$ microstructures in Ti alloys. They also show that this mechanism operates in a rather narrow processing window. However, the newest PANDAT thermodynamic database[46–48] for the $\beta$ phase in Ti-Mo shows the existence of a true miscibility gap. It is also noted that the predicted $c_0(T)$ values from this new database have changed to ~3.0 and 4.35 (all in wt.% Mo) at 700°C and 600°C, respectively. Using this new thermodynamic database, the predicted microstructural evolution during $\alpha$ precipitation following the pseudo-spinodal mechanism is shown in Fig. 3 when the alloy composition (5.0 wt.% Mo) is greater than, but near, $c_0(T)$ (~3.0 wt.% Mo). The compositional fluctuations within the $\beta$ matrix (again simulated by the Langevin noises[43]) in both concentration and structural order parameters (Fig. 3a and a′, which were turned off after the reduced time $t^* = 20$) could result in the composition of certain volume elements being leaner in solute than the $c_0(T)$ point. These regions transform congruently to the $\alpha$ phase (see Fig. 3b and b′) but with concentrations far from equilibrium (see Fig. 3e). Subsequently, continuous diffusional partitioning between the $\beta$ and $\alpha$ phases drives their compositions toward equilibrium as in spinodal decomposition (see Fig. 3e). The concentration variation shown in Fig. 3e is consistent with that measured using atom-probe tomography in Ti-5553.[17]

The existence of a miscibility gap in $\beta$ of Ti-Mo system (see Fig. 4)[46–48] and other Ti alloys[49] provides a new opportunity to use a different non-conventional transformation pathway, i.e., precursory phase separation, to engineer ultrafine $\alpha + \beta$ microstructures in much wider composition ranges.

This mechanism could also explain the experimental observations presented in Fig. 2. According to the latest database,[46–48] the ultrafine microstructure observed in Ti-10Mo at 600°C (Fig. 2c′ and d′) may not be produced by the pseudo-spinodal mechanism because the alloy composition is too far away from $c_0$ (e.g., $c - c_0 = 5.65$ wt.%), but it could be attributed to the precursory phase separation by spinodal decomposition. For example, if an alloy is held within the spinodal region of the miscibility gap and above the $\beta$-transus, then true spinodal decomposition (rather than pseudo-spinodal decomposition) will take place in $\beta$ (it may also take place during cooling toward the $\beta$-transus), producing concentration modulations prior to $\alpha$ precipitation, with $\beta$-stabilizer rich and lean regions on a very fine scale. Such a precursory phase separation may also produce many pockets in the parent phase whose compositions cross the $c_0(T)$ point, thus leading to congruent transformation proceeding decomposition. This transformation pathway is similar to the pseudo-spinodal pathway and therefore could lead to ultrafine and ultrauniform intragranular $\alpha + \beta$ microstructures. Our phase-field simulation results (Fig. 5a–c) obtained for such a system have confirmed this analysis.[50] Different from the pseudo-spinodal mechanism, this precusary spinodal decomposition mechanism operates within a much wider composition range. Our experimental observations have confirmed that refined $\alpha + \beta$ microstructures containing intragranular $\alpha$ precipitates in Ti-Mo can be obtained in a wide composition range (Fig. 5d–f).[50]

When there is a miscibility gap in the parent phase, both pseudo-spinodal and precursory spinodal transformation pathways may exist, which can be illustrated in reference to the free energy curves drawn schematically in Fig. 6. Figure 6a describes the pseudo-spinodal mechanism with alloy composition $c$ being close to $c_0$ but far away from the spinodal region, a situation corresponding to rela-

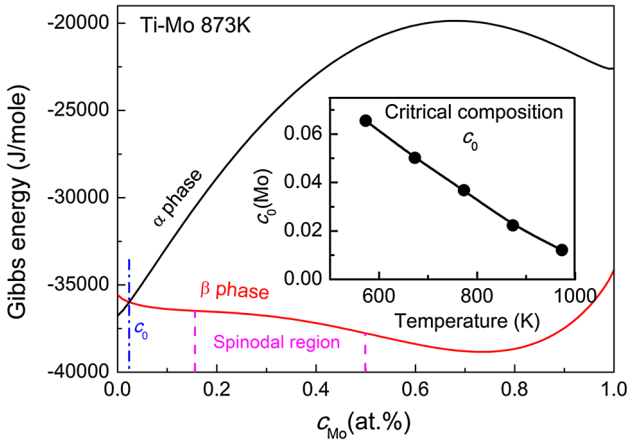


Fig. 4. Gibbs free energy curves of $\alpha$ and $\beta$ phases in Ti-Mo at 873 K based on PANDAT database. There is a spinodal region between $c = 0.15$ and $c = 0.5$. The intersection between the free energy curves defines the critical concentration $c_0$. The inset shows $c_0$ as a function of temperature.

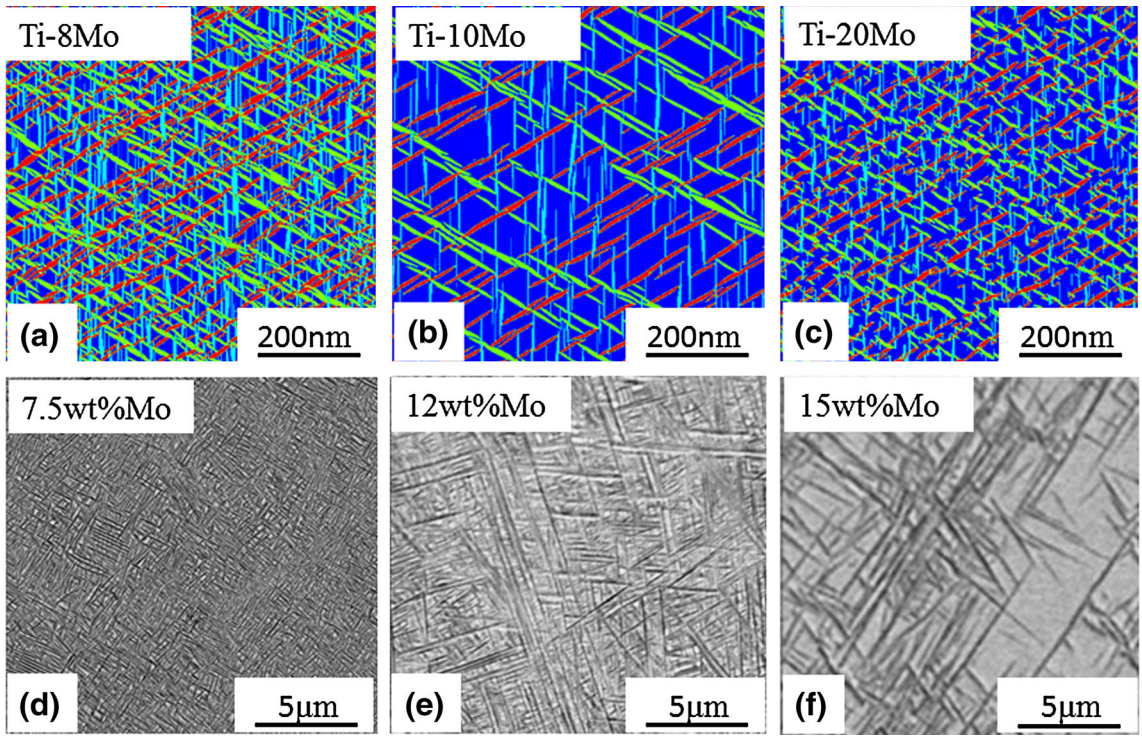


Fig. 5. $\alpha + \beta$ microstructures predicted by two-dimensional phase-field simulations for (a) Ti-8Mo, (b) Ti-10Mo, and (c) Ti-20Mo at 573 K. Experimental observations of $\alpha + \beta$ microstructures for (d) Ti-7.5Mo, (e) Ti-12Mo, and (f) Ti-15Mo at 873 K.

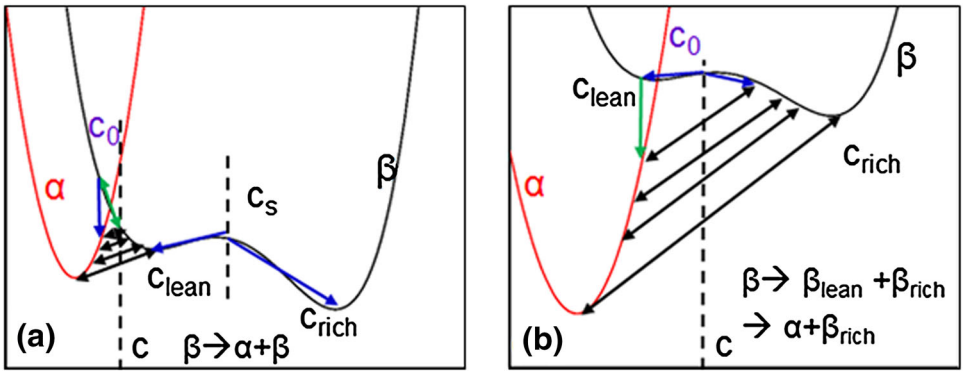


Fig. 6. Schematic free energy curves for non-conventional transformation pathways in Ti alloys: (a) Pseudo-spinodal mechanism and (b) precursory spinodal mechanism. See text for more details.

tively high temperatures for Ti-Mo. In this case, the nonconventional intragranular transformation pathway can be realized only within a narrow composition range. Figure 6b describes the precursory spinodal decomposition mechanism. It corresponds to relatively low temperatures for Ti-Mo where $c_0(T)$ is relatively high and close to the spinodal region. In this case, the pseudo-spinodal mechanism will operate directly when the alloy composition is close to $c_0(T)$ and the precursory spinodal mechanism will operate when the alloy composition is far from $c_0(T)$ but within the spinodal region (which is relatively large).

## CONTROL OF TRANSFORMATION TEXTURE

As noted previously, during TMP many factors can lead to the occurrence of variant selection during the $\beta$-to-$\alpha$ transformation and formation of microtexture. For both $\beta$ and $\alpha + \beta$ processing routes, the $\beta \rightarrow \alpha$ transformation starts from prior $\beta$ grain boundaries that have strong preference to select certain variants for allotriomorphic $\alpha$ (GB$\alpha$).[13,51] Colony $\alpha$, i.e., a cluster of parallel $\alpha$ plates belonging to a single variant (the same variant as the GB$\alpha$) could then develop into the $\beta$ grain that holds a Burgers orientation relationship (BOR)[52] with the GB$\alpha$.[13,53–56] The development of colony structures on the other adjacent $\beta$ grain is also subjected to the influence of the GB$\alpha$.[12,13,53,56] The nonconventional intragranular transformation pathways discussed above may serve as an effective means to eliminate such variant selection processes.

Defects such as dislocations and stacking faults generated during TMP in either the $\beta$ or the $\alpha + \beta$ phase region may act as preferred nucleation sites for a specific subset of $\alpha$ variants. As an example, the results obtained from a recent phase-field simulation study of $\beta \rightarrow \alpha$ transformation in Ti-6Al-4V in the presence of a single edge-type dislocation of the $(12\bar{1})[\bar{1}11]_\beta$ slip system is shown in Fig. 7.[57] It is readily seen that variants V1 and V7[38] nucleate first along the dislocation line and develop into laths during growth. This is because the habit planes of these $\alpha$ variants contain the dislocation line. During the growth of V1 and V7, variants V4 and V6 are further selected by V1 and V7, forming an alternative arrangement on the broad faces of these primary $\alpha$ laths. This autocatalytic process leads to the formation of closed-triangular patterns, frequently observed in the experiments,[11] consisting of three $\alpha$ variants sharing a common $\langle 11\bar{2}0_\alpha \rangle$ direction.[38,57] Concurrently, variants V10 and V12 are formed on the broad face of V7 in the form of thin laths.

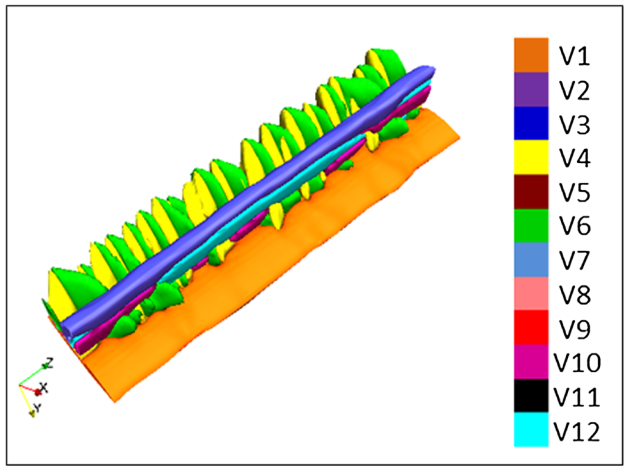


Fig. 7. Phase-field simulation of variant selection due to a single straight edge-dislocation belonging to $(12\bar{1})[\bar{1}11]_\beta$ slip system. In the figure, the dislocation line is along $z \| [\bar{1}11]_\beta$.

Besides dislocations, there exists a rich variety of other sources that generate local stresses and could lead to variant selection within a sample during TMP. For example, owing to the anisotropy of thermal expansion in the $\alpha$ phase (which is 20% larger in the $\langle c \rangle$ direction than in the $\langle a \rangle$ directions), substantial residual stresses are common in $\alpha + \beta$ Ti alloys even after a stress-relief annealing treatment.[58–60] Moreover, local stress fields will also be generated by $\alpha$ precipitation and autocatalysis has been shown frequently to cause variant selection.[11,61] Furthermore, for polycrystalline materials

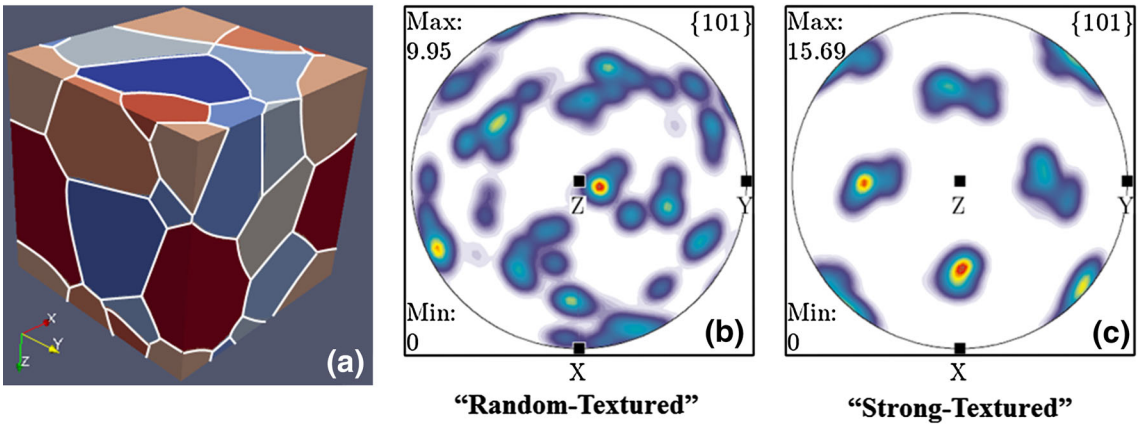


Fig. 8. (a) Polycrystalline $\beta$ matrix with two different strengths of starting $\beta$ texture: random textured (b) and strong textured (c) as indicated by the maxima intensity in the $\{101\}_\beta$ pole figures.

under an external stress or strain field, the local stress state within the sample will vary significantly from grain to grain because of the elastic anisotropy in each grain that leads to elastic inhomogeneity in the sample.[62] It is clear that the local stress state, due to a rich variety of sources, is a key factor in controlling variant selection and hence the final transformation texture during $\alpha$ precipitation in $\alpha + \beta$ Ti alloys.

To demonstrate how certain constraints and stress conditions experienced by a component during TMP affect variant selection and formation of microtexture, we have performed three-dimensional (3-D) phase-field simulations under different types of uniform prestrains that are realized by applying an external load to a sample and then clamping the sample. Such a boundary condition parallels to the recent experimental study on variant selection in Ti-6Al-4V.[63] A polycrystalline sample of Ti-6Al-4V (Fig. 8a) is created by the Voronoi algorithm and relaxed by a phase-field grain growth code[64] to obtain equilibrium junctions among $\beta$ grains. The orientation of each $\beta$ grain with respect to the sample reference is specified by a set of Euler angles $[\phi_1, \Phi, \phi_2]$ using the Bunge notation.[39] The ODFs of $\beta$ texture are then obtained from individual orientation data using MTEX MATLAB quantitative texture analysis software.[65] The chosen kernel is a de la Vallée Poussin kernel with a smoothing half-width of 5°. The beta texture is represented by the $\{101\}_\beta$ pole figures shown in Fig. 8, whose intensity contours are represented in times-random units. For convenience, the freely available MTEX MATLAB toolbox for quantitative texture analysis[65] is used to make all pole figures. Because the starting texture of the $\beta$ phase has a strong influence on the transformation texture of the $\alpha$ phase because of the BOR between the two phases, two sets of initial $\beta$ textures are considered in the current study. One has a relatively random texture and is referred to as "randomly textured" sample, and the other has a relatively strong texture and is referred to as "strongly textured" sample.[63] Their textures are represented by the $\{101\}_\beta$ pole figures shown in Fig. 8b and c, respectively. As can be seen from the pole figures, the strongly textured sample has a relatively larger maximum pole intensity of the $\{101\}_\beta$ pole than that of the randomly textured one.

Within each $\beta$ grain, 12 nonconserved phase-field-order parameters are employed to describe the spatial distributions of all 12 $\alpha$ variants.[38] As such, it requires $12 \times N$ order parameters in total to describe $\alpha$ precipitation in a polycrystalline $\beta$ sample consisting of $N$ grains. Variant selection behavior under the influence of both starting $\beta$ texture and prestrain are then investigated using a quantitative 3-D phase-field model. The nonuniform stress field within the elastically inhomogeneous polycrystalline sample under a prestrain is obtained by a phase-field model with inhomogeneous elastic moduli[62] and is updated in parallel to $\alpha$ precipitation.

For the randomly textured $\beta$ sample, when the prestrain is introduced by a compressive stress that is applied along the $x$-axis before the system's boundary is clamped, we can see clearly from Fig. 9a that the precipitation behaviors of different $\alpha$ variants vary significantly from one $\beta$ grain to another. In some grains, multiple $\alpha$ variants appear simultaneously, while in some others only limited numbers of $\alpha$ variants are present. The volume fraction of the total $\alpha$ phase in each $\beta$ grain also varies significantly from grain to grain. The overall microstructures of $\alpha$ precipitates within individual $\beta$ grains also vary significantly when different types of prestrains are introduced to the random-textured sample as shown in Fig. 9b. Similar variant selection behavior is also observed in the strongly textured sample (Fig. 9c and d).

In order to quantify the texture evolution during $\alpha$ precipitation, a virtual EBSD scan is preformed through the sample to read the orientation information of individual $\alpha$ precipitates according to the index of the $\alpha$ variants[38] and orientation of the $\beta$ matrix based on the BOR. The ODFs for the $\alpha$ phase

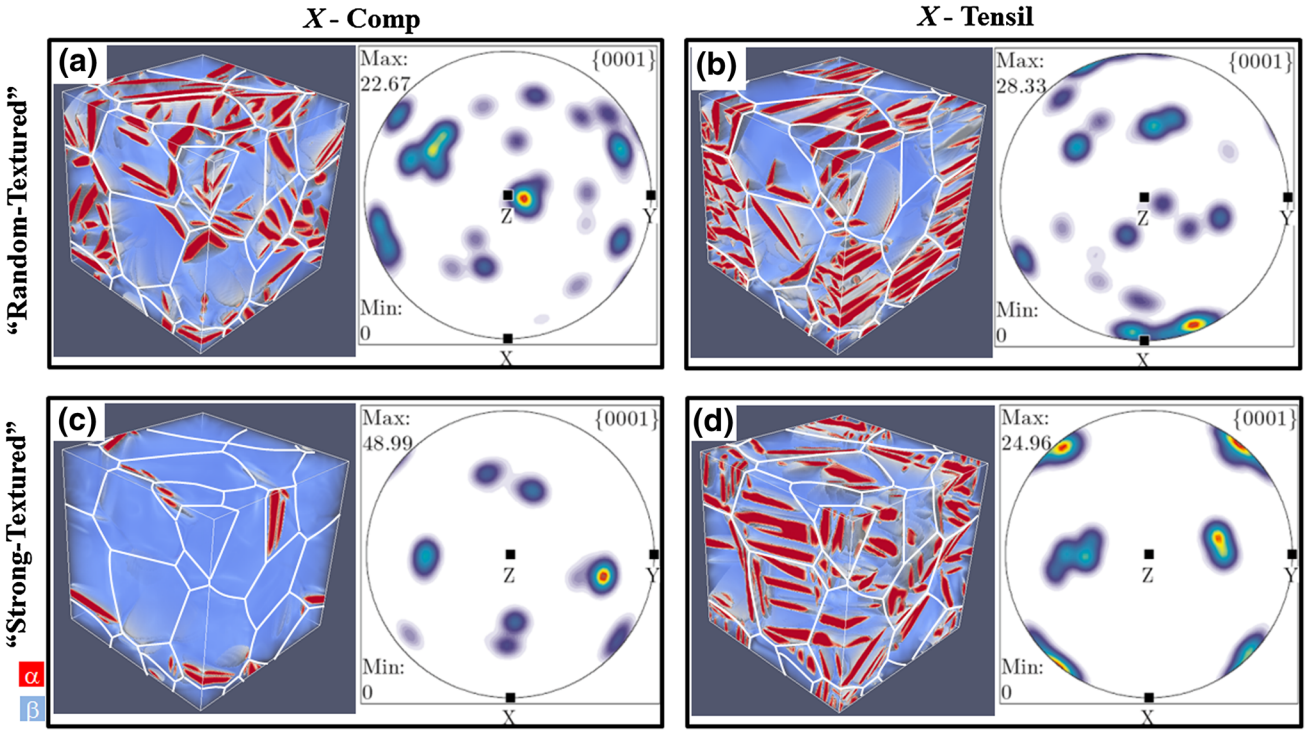


Fig. 9. Phase-field simulations of $\alpha$ precipitation in a polycrystalline $\beta$ sample, showing the effects of both starting $\beta$ texture and prestrain on the microstructure and transformation texture (represented by the $(0001)_\alpha$ pole figure).

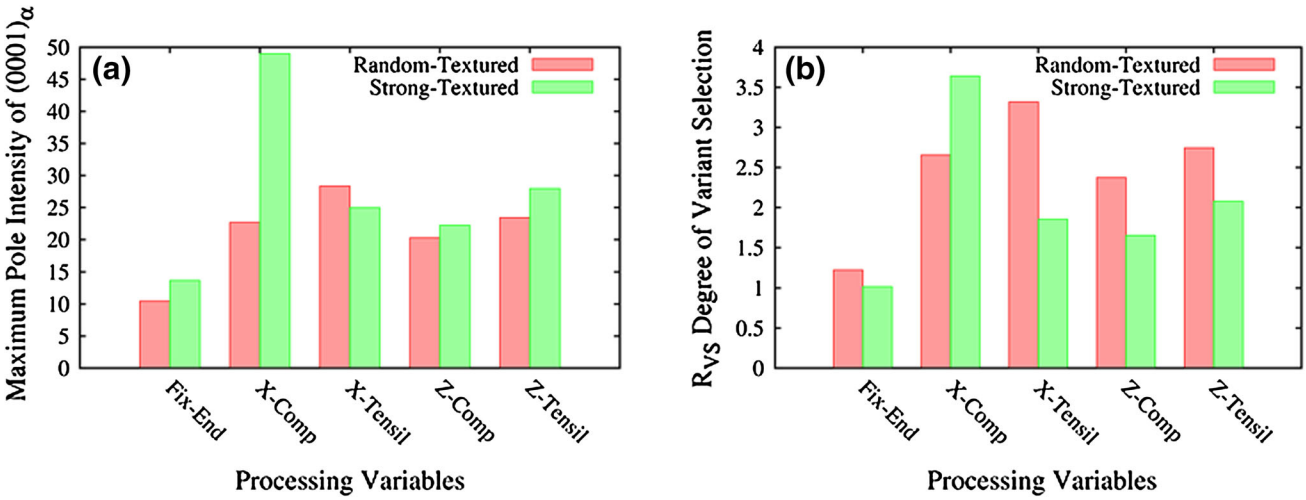


Fig. 10. Influence of both starting $\beta$ texture and type of prestrain on (a) the strength of final $\alpha$ texture and (b) degree of variant selection $R_{VS}$.

are obtained using the same approach as that used in quantifying the $\beta$ texture.[40] The final $\alpha$ textures are represented by the $(0001)_\alpha$ pole figures in Fig. 9. The strength of the transformed $\alpha$ texture is simply represented by the texture-component maxima in these pole figures, which indicate that the strength of the transformation texture depends on both the starting $\beta$ texture and the type of prestrain. It is generally believed that the stronger is the starting $\beta$ texture, the stronger is the final $\alpha$ texture, which is also true in most of the cases considered in our simulations. However, when the prestrain is generated via a 50-MPa tensile stress, the final maximum intensity of the basal pole in the strongly textured sample is smaller than that in the randomly textured sample, as shown in Fig. 10a. The differences in both microstructure and texture reflect different variant selection behaviors under the combined effect of the starting $\beta$ texture and the evolution of the $\alpha$ precipitate microstructure due to the specific prestrain.

The degree of variant selection could be quantified using the ratio $R_{VS}$ between the maxima-pole intensities in the $(0001)_\alpha$ and $\{011\}_\beta$ pole figures.[63] It

has been shown that, if there is no variant selection; i.e., the orientation density of $\beta$ is distributed equally to all 12 $\alpha$ variants in each $\beta$ grain, then the corresponding $\{101\}_\beta$ and $(0001)_\alpha$ pole figures will be identical and $R_{VS} \equiv 1$. If variant selection occurs, then $R_{VS} > 1$. It can be seen from Fig. 10b that $R_{VS}$ in the strongly textured sample is smaller than that in the randomly textured sample except when the prestrain is associated with a compression along the $x$ direction. Thus for samples with strong $\beta$-texture, certain prestraining before the $\beta \rightarrow \alpha$ transformation could result in the maximum number of $\alpha$ variants and hence avoid or reduce microtexture at both the individual $\beta$ grain level and the overall polycrystalline sample level. The effects of different processing variables such as cooling rate, residual stress, prestrain, type of boundary constraint, and preexisting microstructure on transformation texture are currently being investigated systematically using the phase-field method, and the simulation results could provide a foundation for microtexture control during TMP of Ti alloys.

## SLIP TRANSMISSION OF DISLOCATION THROUGH *A*/*B* INTERFACES

As noted earlier, the density and nature of heterophase interfaces and their spatial uniformity are keys in determining the deformation mechanisms and mechanical behavior of precipitation-hardened alloys such as the $\alpha + \beta$ Ti alloys. Following our recent success[66–71] in studying dislocation interactions with $\gamma/\gamma'$ microstructures in Ni-base superalloys using the microscopic phase-field dislocation model[72–75] in combination with ab initio calculations of GSF energy, a quantitative phase-field model of dislocation—$\alpha/\beta$ microstructure interactions has been formulated for a model $\alpha + \beta$ Ti alloy, using as model inputs the elastic constants of $\alpha$ and $\beta$ phases and GSF energies of operating slip systems in both $\alpha$ (e.g., $\langle a \rangle$ type dislocations on the basal plane) and $\beta$ (e.g., $1/2\langle 111 \rangle$on $\{110\}$) phases obtained from the ab initio calculations.[76] The model is being used to investigate the critical resolved shear stresses, $\tau_{CRSS}$, for dislocations to pass through the various $\alpha/\beta$ microstructures generated by both conventional and nonconventional transformation pathways. Such a study will allow us to identify critical microstructural features and construct microstructure-sensitive property models using dislocation density-based crystal plasticity models.[77–79] Serious efforts are also being made to couple directly the phase-field model of alpha/beta microstructure evolution and the crystal plasticity model of dislocation structure evolution. For example, to develop a microstructure-sensitive dislocation density-based crystal plasticity model, the detailed deformation mechanisms for a given $\alpha + \beta$ microstructure need to be incorporated in the constitutive hardening equations. The details of how individual dislocations interact with $\alpha/\beta$ interfaces enabled by the microscopic phase field models will serve as critical input to such a crystal plasticity models that are currently under being development at several places. Serious efforts are also being made to couple directly the phase-field model of $\alpha/\beta$ microstructure evolution and the crystal plasticity model of dislocation structure evolution.[77–79]

## CONCLUSION

The integrated CALPHAD and phase-field modeling approach has been shown to be effective in exploring new transformation pathways and novel alloy design ideas. The approach identified two nonconventional intragranular transformation pathways, i.e., the pseudo-spinodal and precursory spinodal pathways in Ti-Mo binary system that led to an extremely refined and uniform $\alpha + \beta$ microstructure. It predicted conditions for these two mechanisms to operate in a given alloy system and demonstrated the importance of accurate thermodynamic databases. For example, the pseudo-spinodal mechanism can operate in systems with and without a miscibility gap, but the alloy composition has to be in close proximity of to the $c_0(T)$ ($\sim$2 wt.%), while the precursory spinodal mechanism can operate in a much broader composition range but requires the presence of a miscibility gap in the parent phase. These simulation predictions have been confirmed by direct experimental observations made on the same alloy system. These intragranular transformation pathways could also be effective means in eliminating microtexture related to variant selection during $\beta \rightarrow \alpha$ transformation via the conventional intergranular transformation pathway.

When certain defects and residual stresses exist in the $\beta$-phase matrix because of TMP, the variant selection process can be predicted fairly accurately by the phase-field simulations, and hence certain measures could be taken to reduce the degree of microtexture.

Although the examples presented in the current work are mostly for a simple binary alloy system, the $c_0(T)$ can be calculated routinely from CALPHAD databases such as PanTi[48] for commercial Ti alloys. Therefore, such an ICME approach may accelerate the exploitation of these nonconventional transformation mechanisms and alloy design concepts, and control of texture, for the development of new Ti alloys having ultrafine and ultrauniform $\alpha + \beta$ microstructures with much improved properties.

## ACKNOWLEDGEMENTS

We acknowledge the support of U.S. Air Force Research Laboratory (AFRL contract FA8650-08-C-5226) and the U.S. National Science Foundation (DMR 1006487 to R.B and H.L.F and DMR1008349 to Y.W). The simulations were partially performed

on supercomputers at Ohio Supercomputing Center and Arctic Region Supercomputing Center.

## REFERENCES


1. J.B. Clark and A.J. Mcevily, *Acta Metall. Mater.* 12, 1359 (1964).
2. W.F. Miao and D.E. Laughlin, *Scr. Mater.* 40, 873 (1999).
3. M.E. Fine, *Metall. Trans. A* 6, 625 (1975).
4. Y.J. Li, P. Choi, C. Borchers, S. Westerkamp, S. Goto, D. Raabe, and R. Kirchheim, *Acta Mater.* 59, 3965 (2011).
5. Y.J. Li, P. Choi, S. Goto, C. Borchers, D. Raabe, and R. Kirchheim, *Acta Mater.* 60, 4005 (2012).
6. H.K.D.H. Bhadeshia and P. Roy, *Soc. A Math. Phys.* 466, 3 (2010).
7. A. Lasalmonie and J.L. Strudel, *Philos. Mag.* 32, 937 (1975).
8. G. Leverant and B. Kear, *Metall. Trans. B* 1, 491 (1970).
9. T. Ahmed and H.J. Rack, *Mater. Sci. Eng. A Struct.* 243, 206 (1998).
10. T. Duerij and J.C. Williams, *Beta Titanium Alloys in the 80's: Proceedings of a Symposium* (Atlanta, GA: Metallurgical Society of AIME, 1984), p. 19.
11. S. Kar, R. Banerjee, E. Lee, and H.L. Fraser, *Solid–Solid Phase Transformation in Inorganic Materials*, ed. J.M. Howe (Warrendale, PA: TMS, 2005).
12. R. Shi, V. Dixit, H.L. Fraser, and Y. Wang, *Acta Mater.* (2014). doi:10.1016/j.actamat.2014.05.003.
13. D. Banerjee and J.C. Williams, *Acta Mater.* 61, 844 (2013).
14. R. Whittaker, K. Fox, and A. Walker, *Mater. Sci. Tech. Ser.* 26, 676 (2010).
15. Y. Ni and A.G. Khachaturyan, *Nat. Mater.* 8, 410 (2009).
16. A. Boyne, D. Wang, R.P. Shi, Y. Zheng, A. Behera, S. Nag, J.S. Tiley, H.L. Fraser, R. Banerjee, and Y. Wang, *Acta Mater.* 64, 188 (2014).
17. S. Nag, Y. Zheng, R.E.A. Williams, A. Devaraj, A. Boyne, Y. Wang, P.C. Collins, G.B. Viswanathan, J.S. Tiley, B.C. Muddle, R. Banerjee, and H.L. Fraser, *Acta Mater.* 60, 6247 (2012).
18. W. Soffa and D. Laughlin, *Proceedings of an International Conference on Solid to Solid Phase Transformations* (Warrendale, PA: The Metallurgical Society of AIME, 1982), p. 159.
19. J.W. Cahn and J.E. Hilliard, *J. Chem. Phys.* 28, 258 (1958).
20. L.D. Landau and E. Lifshitz, *Phys. Z. Sowjetunion* 8, 101 (1935).
21. J.S. Rowlinson, *J. Stat. Phys.* 20, 197 (1979).
22. J.D. Eshelby, Proc. Roy. Soc. Lond. A Matter. 241 (1957).
23. J.D. Eshelby, *Proc. R. Soc. A* 252, 561 (1959).
24. A. Khachaturyan, *Sov. Phys. Sol. State* 8, 2163 (1967).
25. A.G. Khachaturyan, *Theory of Structural Transformations in Solids* (New York: Wiley, 1983).
26. A.G. Khachaturyan and G.A. Shatalov, *Sov. Phys. Sol. State.* 11, 118 (1969).
27. W.J. Boettinger, J.A. Warren, C. Beckermann, and A. Karma, *Annu. Rev. Mater. Sci.* 32, 163 (2002).
28. L.-Q. Chen, *Annu. Rev. Mater. Sci.* 32, 113 (2002).
29. H. Emmerich, *The Diffuse Interface Approach in Materials Science: Thermodynamic Concepts and Applications of Phase-Field Models* (New York: Springer, 2003).
30. A. Karma, *Encyclopedia of Materials: Science and Technology*, Vol. 2, ed. K.H.J. Buschow (Oxford, U.K: Elsevier, 2001), p. 6873.
31. C. Shen and Y. Wang, *Handbook of Materials Modeling*, ed. S. Yip (New York: Springer, 2005), p. 2117.
32. Y. Wang, L.Q. Chen, and N. Zhou, *Characterization of Materials* (New York: Wiley, 2012).
33. Y.U. Wang, Y.M. Jin, and A.G. Khachaturyan, *Handbook of Materials Modeling* (New York: Springer, 2005), p. 2287.
34. L.-Q. Chen and A.G. Khachaturyan, *Acta Metall. Mater.* 39, 2533 (1991).
35. R. Shi, N. Ma, and Y. Wang, *Acta Mater.* 60, 4172 (2012).
36. Y. Wang, N. Ma, Q. Chen, F. Zhang, S.L. Chen, and Y.A. Chang, *JOM J. Min. Metal. Mater. S.* 57, 32 (2005).
37. Q. Chen, N. Ma, K.S. Wu, and Y.Z. Wang, *Scr. Mater.* 50, 471 (2004).
38. R. Shi and Y. Wang, *Acta Mater.* 61, 6006 (2013).
39. H.J. Bunge, *Texture analysis in materials science–mathematical methods* (London, U.K.: Butterworth-Heinemann, 1982).
40. R. Shi and Y. Wang, *Acta Mater.* (2014, in press).
41. H.L. Lukas, S.G. Fries, and B. Sundman, *Computational Thermodynamics: The CALPHAD Method* (Cambridge, U.K.: Cambridge University Press, 2007), p. 10.
42. W. Cao, S.L. Chen, F. Zhang, K. Wu, Y. Yang, Y.A. Chang, R. Schmid-Fetzer, and W.A. Oates, *CALPHAD* 33, 328 (2009).
43. C. Shen, J.P. Simmons, and Y. Wang, *Acta Mater.* 55, 1457 (2007).
44. Y.J. Liu, L.J. Zhang, and D. Yu, *J. Phase Equilib. Diff.* 30, 334 (2009).
45. R.W. Balluffi, S.A. Allen, and W.C. Carter, *Kinetics of Materials* (Hoboken, NJ: Wiley, 2005).
46. S.L. Chen, F. Zhang, F.Y. Xie, S. Daniel, X.Y. Yan, Y.A. Chang, R. Schmid-Fetzer, and W.A. Oates, *JOM* 55, 48 (2003).
47. J. Shim, C. Oh, and D. Lee, *Metall. Mater. Trans. B* 27, 955 (1996).
48. CompuTherm, PanTitanium, http://www.computherm.com/index.php?route=product/product&path=59_83&product_id=28.
49. E.S.K. Menon and H.I. Aaronson, *Acta Metall. Mater.* 34, 1963 (1986).
50. D. Wang, Y. Zheng, R. Shi, R. Banerjee, H.L. Fraser, and Y. Wang, *Acta Mater.* (2014, in press).
51. G. Lutjering and J.C. Williams, *Titanium (Engineering Materials and Processes)* (Berlin, Germany: Springer, 2007).
52. W.G. Burgers, *Physica* 1, 561 (1934).
53. D. Bhattacharyya, G.B. Viswanathan, R. Denkenberger, D. Furrer, and H.L. Fraser, *Acta Mater.* 51, 4679 (2003).
54. D. Bhattacharyya, G.B. Viswanathan, and H.L. Fraser, *Acta Mater.* 55, 6765 (2007).
55. N. Stanford and P.S. Bate, *Acta Mater.* 52, 5215 (2004).
56. S.M.C. van Bohemen, A. Kamp, R.H. Petrov, L.A.I. Kestens, and J. Sietsma, *Acta Mater.* 56, 5907 (2008).
57. D. Qiu, R. Shi, D. Zhang, W. Lu, and Y. Wang, *Acta Mater.* (2014, in press).
58. G.A. Sargent, K.T. Kinsel, A.L. Pilchak, A.A. Salem, and S.L. Semiatin, *Metall. Mater. Trans. A* 43A, 3570 (2012).
59. R.A. Winholtz, *Encyclopedia of Materials: Science and Technology*, ed. K.H.J. Buschow (Oxford, UK: Elsevier, 2001), p. 8148.
60. L. Zeng and T.R. Bieler, *Mater. Sci. Eng. A Struct.* 392, 403 (2005).
61. E. Lee, R. Banerjee, S. Kar, D. Bhattacharyya, and H.L. Fraser, *Philos. Mag.* 87, 3615 (2007).
62. Y.U. Wang, Y.M. Jin, and A.G. Khachaturyan, *Appl. Phys. Lett.* 80, 4513 (2002).
63. S.L. Semiatin, K.T. Kinsel, A.L. Pilchak, and G.A. Sargent, *Metall. Mater. Trans. A* 44, 3852 (2013).
64. J. Gruber, N. Ma, Y. Wang, A.D. Rollett, and G.S. Rohrer, *Model. Simul. Mater. Sci.* 14, 1189 (2006).
65. F. Bachmann, R. Hielscher, and H. Schaeben, *Solid State Phenom.* 160, 63 (2010).
66. L. Kovarik, R.R. Unocic, J. Li, P. Sarosi, C. Shen, Y. Wang, and M.J. Mills, *Prog. Mater. Sci.* 54, 839 (2009).
67. N. Zhou, C. Shen, M.J. Mills, J. Li, and Y. Wang, *Acta Mater.* 59, 3484 (2011).
68. V.A. Vorontsov, C. Shen, Y. Wang, D. Dye, and C.M.F. Rae, *Acta Mater.* 58, 4110 (2010).
69. N. Zhou, C. Shen, M. Mills, and Y. Wang, *Philos. Mag.* 90, 405 (2010).
70. N. Zhou, C. Shen, P.M. Sarosi, M.J. Mills, T. Pollock, and Y. Wang, *Mater. Sci. Technol. Ser.* 25, 205 (2009).
71. R.R. Unocic, N. Zhou, L. Kovarik, C. Shen, Y. Wang, and M.J. Mills, *Acta Mater.* 59, 7325 (2011).

72. Y. Wang, Y. Jin, and A. Khachaturyan, *Dislocation Dynamics: Phase Field* (Dordrecht, The Netherlands: Springer, 2005).
73. Y. Wang and J. Li, *Acta Mater.* 58, 1212 (2010).
74. C. Shen and Y. Wang, *Acta Mater.* 52, 683 (2004).
75. C. Shen and Y. Wang, *Acta Mater.* 51, 2595 (2003).
76. S. Chen, J. Li, and Y. Wang, *Acta Mater*. 74, 125 (2014).
77. A. Arsenlis, D.M. Parks, R. Becker, and V.V. Bulatov, *J. Mech. Phys. Solids* 52, 1213 (2004).
78. A. Ma, F. Roters, and D. Raabe, *Acta Mater.* 54, 2169 (2006).
79. I.J. Beyerlein and C.N. Tome, *Int. J. Plastic.* 24, 867 (2008).